Exploring Precision Polymers to Fine-tune Magnetic Resonance Imaging Properties of Iron oxide Nanoparticles

Aaron M. King,[a] Caroline Bray,[b] Stephen C. L. Hall,[b] Joseph C. Bear,[c] Lara K. Bogart,[d] Sebastien Perrier,[b] and Gemma-Louise Davies[c]*

a Department of Chemistry, University College London, 20 Gordon Street, London WC1H 0AJ, U.K

b Department of Chemistry, University of Warwick, Gibbet Hill Road, Coventry CV4 7AL, U.K

c School of Life Science, Pharmacy and Chemistry, Kingston University, Penryhn Road, Kingston-upon-Thames, KT1 2EE, U.K

d UCL Healthcare Biomagnetics Laboratory, 21 Albemarle Street, London W1S 4BS, U.K

Corresponding Author: Gemma-Louise Davies (email: gemma-louise-davies@ucl.ac.uk)

Abstract

The use of bio-polymers as stabilising agents for iron oxide-based negative magnetic resonance imaging (MRI) contrast agents has become popular in recent years, however the wide polydispersity of biologically-derived and commercially available polymers limits the ability to produce truly tuneable and reproducible behaviour, a major challenge in this area. In this work, stable colloids of maghemite/magnetite nanoparticles were prepared utilising precision-engineered bio-polymer mimics, poly(2-acrylamido-2-methylpropane sodium sulfonate) (P(AMPS) polymers, with controlled narrow polydispersity molecular weights, as templating stabilisers. In addition to producing magnetic colloids with excellent MRI contrast capabilities (r_2 values reaching 434.2 $mM^{-1}s^{-1}$ at 25 °C and 23 MHz, several times higher than similar commercial analogues), variable field relaxometry provided unexpected important insights into the dynamic environment of the hydrated materials, and hence their exceptional MRI behaviour. Thanks to the polymer's templating backbone and flexible conformation in aqueous suspension, nanocomposites appear to behave as "multi-core" clustered species, enhancing interparticle interactions whilst retaining water diffusion, boosting relaxation properties at low frequency. This clustering behaviour, evidenced by Small-angle X-ray scattering, and hence relaxometric response, was fine-tuned using the well-defined molecular weight polymer species with precise iron to polymer ratios. By also showing negligible haemolytic activity, these nanocomposites exhibit considerable potential for MRI diagnostics.

Introduction

Superparamagnetic iron oxide nanoparticles (SPIONs) have been a major research focus for a number of years, with applications ranging catalysis, environmental remediation, magnetically triggered reactions, cell labelling and bioseparation, biosensing, magnetic resonance imaging (MRI), and magnetic hyperthermia therapy.[1–7] Their diverse applications stem from their unique size-dependent magnetic properties, which are tuneable thanks to their (relatively) straight-forward synthesis and surface modification.[8] Interest in their use as MRI contrast agents has been steady over the past few

decades thanks to their biocompatibility and clinical application. As a useful non-invasive imaging tool, MRI is valuable in the diagnosis and monitoring of disease. Its potency can be enhanced through the application of contrast agents (CAs), which boost MRI signal contrast by decreasing indigenous water proton relaxation times through close molecular interactions, described in detail by the Solomon, Bloembergen and Morgan (SBM) equations.[9–11] So-called positive CAs, usually based on paramagnetic Gd^{3+} chelates such as Magnevist® or Dotarem®, predominantly accelerate longitudinal relaxation times (T_1), producing hyperintense signal. Negative CAs, on the other hand, principally enhance transverse relaxation times (T_2), and are typically composed of stabilised superparamagnetic iron oxide nanoparticles, for example Feridex®, Resovist®, and Sinerem®, and provide regions of hypointense signal.[12–15]

Although Gd^{3+}-based CAs have traditionally been more popular clinically due to the 'brightened' images they can provide, their use has been increasingly associated with significant risks such as nephrogenic systemic fibrosis (NSF), particularly towards patients with renal insufficiency, and more recently have been reported to accumulate in the brain.[16,17] Whilst 'uncoated' iron oxide nanoparticles have been shown to exhibit low levels of toxicity, particles stabilised with a biocompatible polymer have been found to be relatively non-toxic. For example, commercially-available dextran coated superparamagnetic iron oxide nanoparticles, Ferumoxtran-10, were demonstrated to be non-toxic to human monocyte macrophages at concentrations as high as 1 mg/ml.[18] Iron oxide based MRI contrast agents have been widely used clinically for imaging the gastrointestinal tract, colon, liver, spleen, and lymph nodes.[10,19–21] Although their clinical MRI use in recent years has decreased (with some negative contrast agents being removed from the market), there remain a number of iron oxide particle-based products in active clinical use, including Lumirem® (for imaging the GI tract) and Feraheme® (a treatment for anaemia).[13,15,22] They additionally remain popular in research due to their unique properties which make them useful for applications such as targeted magnetic hyperthermia, drug delivery, cell tracking, and MRI contrast enhancement.[23–28]

Recent years have seen a significant amount of research towards high performance MRI CAs exploiting the tuneable properties of nanoparticles.[9,29–32] Excellent colloidal stability, magnetic properties, and well hydrated and biocompatible surfaces are the key characteristics of high performing nanostructured contrast agents. Advances in both the synthesis of the magnetic iron oxide core, and the functionalization of the particle surface, has led to a series of magnetic particle-based contrast agents with strong and tuneable MRI signal.[33–37] Polymeric stabilisation of negative contrast agents can be carried out through (covalently or non-covalently) associating polymers (*e.g.* polyethylene glycol or dextran) on iron oxide particle surfaces after their preparation, or through the *in situ* incorporation of a stabilising polyelectrolyte during nanoparticle preparation.[19,38–41] The latter technique has proven successful in the preparation of contrast agents with excellent colloidal stability and strong contrast enhancement, due to the templating behaviour of some polymer species. For example, DNA, poly(sodium-4-styrene) sulfonate and heparin, have been used to stabilise Fe_3O_4 and $CoFe_2O_4$ particles

following this approach, generating exceptionally high relaxation behaviour.[29,42,43] Key to the strong contrast enhancement reported in these works was the negatively charged polymers used, whose backbones offered sites at which the ferritic nanoparticles could seed and grow, acting as a templating species, as well as colloidal stabilisers. This templating behaviour is responsible for increased magnetic dipole-dipole interactions between neighbouring particles, thereby boosting their relaxation response due to increased anisotropy.[30,43] Whilst the control of particle interaction using templating polymers is an intriguing approach to tuneable contrast agents, commercially-available polymers generally suffer from high polydispersity and poorly controlled molecular weight distributions. This can detrimentally impact reproducibility, as well as provide poor control over the vital interparticle interactions of produced composites, affecting tunability of contrast agent performance.

Recently, carefully controlled molecular weight heparin-mimicking polymers, poly(2-acrylamido-2-methylpropane sodium sulfonate) (P(AMPS)), and their nanovesicle counterparts, have been produced and demonstrated excellent biocompatibility and low haemolytic activity.[44,45] Herein, we aim to exploit these controlled molecular weight linear P(AMPS) polyelectrolytes as stabilising and templating agents to produce families of stable aqueous maghemite/magnetite nanocomposites. These low polydispersity polymers, with controlled numbers of negative sulfonate groups, provide regulation of the templating of magnetic cores at these seeding sites, offering the opportunity for the production of contrast agents with precisely tuneable interparticle interactions and hence MRI contrast behaviour. The proton relaxation enhancement capabilities, at single field and variable field strengths, and haemolytic activity of these composites are assessed towards new families of biocompatible and tuneable MRI contrast agents.

Experimental

All chemicals were used as supplied. $FeCl_2 \cdot 4H_2O$ (≥99.0 %), $FeCl_3 \cdot 6H_2O$ (97 %), ammonium hydroxide (BioUltra 1M), and Xanthan gum (from Xanthomonas campestris) were purchased from Sigma-Aldrich Ltd. Defibrinated sheep's blood, and Triton-X 100 (≥ 98.0 %, molecular biology grade) were purchased from VWR, UK. Sodium 2-acrylamido-2-methylpropane sulfonate (AMPS® 2405, 50 wt% in water) was donated by Lubrizol. Thermal initiator, 2,2′-azobis[2-methyl-N-((2-hydroxyethyl)propionamide] (VA-086, 98%) was obtained from Wako Chem. 2-(((butylthio)-carbonothioyl)thio)-2-methylpropanoic acid (BDMAT) was synthesized using previous literature conditions.[44] Ultrapure water was collected from an Elga PureLab system operated at 15.0 MΩ.

Physical and Structural Characterisation

Transmission electron microscopy (TEM) images were obtained on a Jeol JEM-1200 microscope, 120 kV, operated with a beam current of 80 mA; images were captured using a Gatan Orius 11-megapixel camera. Samples were prepared by deposition and drying of nanoparticle samples (20 μL of

stock stable magnetic fluid suspensions) onto formvar-coated 300-mesh copper TEM grids (EM Resolutions). Diameters were measured using ImageJ software version 1.8; average values were calculated by counting a minimum of 100 particles, with error derived from standard deviation. Magnetically aligned samples were dried in the presence of a parallel permanent magnetic field (2250 Gauss).

Hydrodynamic particle size and zeta potential measurements were determined by dynamic light scattering (DLS) using a Malvern Zetasizer Nano ZS instrument. A 4 mW He-Ne 633 nm laser module was used, and scattered light was measured at 173° (back scattering). The attenuator and position were selected automatically by the instrument and particle sizes reported as the average of at least 4 measurements, with error derived from standard deviation.

Small-angle X-ray scattering (SAXS) measurements were performed using a Xenocs Xeuss 2.0 equipped with a micro-focus Cu K_α source collimated with scatterless slits providing a 0.8 mm diameter beam. Samples measured were stable aqueous washings which were loaded into 1 mm path length borosilicate glass capillaries. SAXS patterns were recorded using a Pilatus 300K detector with a pixel size of 0.172 mm × 0.172 mm. The sample to detector distance was calibrated using silver behenate ($AgC_{22}H_{43}O_2$) providing a value of 2.481(5) m, providing an effective scattering vector, Q, range of 0.005–0.16 $Å^{-1}$ where Q is defined as

$$Q = \frac{4\pi \sin\theta}{\lambda} \tag{1}$$

Where 2θ is the scattering angle and λ is the X-ray wavelength. Data were collected for 4 hours at 25 °C. A radial integration of the 2D scattering profile was performed using FOXTROT software and the resulting data corrected for the absorption, sample thickness and background.[46] Finally, the scattering intensity was then rescaled to absolute intensity using glassy carbon as a standard.[47] SAXS data were analysed using model-dependent analysis implemented within SasView software (www.sasview.org).[48] A model describing a fractal aggregate of spherical particles was used, as has been described in detail elsewhere.[49] The scattering length density (SLD) defining the 'scattering power' of a material, is defined as the sum of X-ray scattering lengths, b_i, of N atoms within a given molecular or particle volume, V_m, as given by

$$SLD = \frac{\sum_{i=1}^{N} b_i}{V_m} \tag{2.1}$$

The SLD of a material can also be calculated using the bulk density, ρ, atomic molar mass, M_i and Avogadro's constant, N_A, where

$$SLD = \frac{\rho N_A \sum_{i=1}^{N} b_i}{\sum_{i=1}^{N} M_i} \tag{2.2}$$

Throughout the fitting procedure, the SLD of water and maghemite/magnetite nanoparticles were calculated as 9.47×10^{-6} Å^{-2} and 41.1×10^{-6} Å^{-2}, respectively, and held constant. Based on nanoparticle dispersity observed by DLS and TEM, a polydispersity was applied to the nanoparticle radius as a Schultz distribution and held at a value of 0.2. All other parameters were permitted to vary throughout the fitting procedure.

Fourier transform infrared (FTIR) spectra were acquired using a Bruker Alpha FTIR spectrometer. A total of 128 scans were collected for solid samples after drying. Raman spectra were collected using a Renishaw Raman inVia microscope with a 633 nm He-Ne excitation laser (0.76 mW when operated at 10% power). Magnetisation measurements were carried out in the range −15 kOe to 15 kOe using a Quantum Design Physical Property Measurement System Vibrating Sample Magnetometer (VSM). Measurements (emu g^{-1}) are based on the total mass of the solid sample, this will include any contribution in mass of the non-magnetic polymer. Powder X-ray diffraction was performed using a Stoe Stadi-P diffractometer with a molybdenum (Mo) X-ray source (50 kV and 30 mA), λ = 0.7093 Å. Two-theta scan range was 2–40.115 ° at a step size of 0.495 ° and 5 seconds per step. Sample holder was a transmission sample holder and samples were prepared using STOE zero scattering foils.

Room temperature (295 ± 5 K) ^{57}Fe Mössbauer spectroscopy was performed using a SeeCo W302 spectrometer (SeeCo Inc., USA) operated in constant acceleration mode. Samples were prepared for measurement by mixing the freeze dried powder with sucrose using a pestle and mortar, to form a paste, which was then mounted in a 2.1 cm coin shaped absorber. Samples were mounted in transmission geometry, with a ^{57}Co in Rh foil as the source of the 14.4 keV γ-rays. Velocity calibration was performed by recording a reference spectrum from a 10 μm thick foil of αFe, also at room temperature. In order to analyse the data, all spectra were folded and baseline corrected using cubic spline parameters derived from fitting the αFe calibration spectrum, following a protocol implemented in the Recoil analysis program.[50] Spectra were least-squares fitted using the 'centre-of-gravity' method, in which Voigtian lineshapes (representing Gaussian distributions of Lorentzian lines) were used in all samples.[51]

Characterisation of Relaxometric Behaviour

Measurement of ^{1}H NMRD profiles was performed on a Stelar Spinmaster FFC2000 1T instrument in the range of 0.01–20 MHz Larmor frequency at two different temperatures (25 °C and 37 °C). The temperature was controlled using a Stelar VTC-91 airflow heater, equipped with a copper-constantan thermocouple; the temperature calibration in the probe head was carried out using a Delta OHM digital thermometer, with an absolute accuracy of 0.5 °C. Fast field cycling (FFC) relaxometry was used to determine the longitudinal relaxation decay over a range of relaxation fields (0.01–40 MHz). A set of 24 relaxation interval values (tau) allowed description of the spin-lattice decay curves for each relaxation field. A standard fitting algorithm (mono-exponential relaxation decay curve) allowed the

evaluation of the relative longitudinal relaxation rate ($R_1 = 1/T_1$), which was converted to relaxivity using Equation (3).

Measurement of r_1 and r_2 values at a fixed field strength were carried out using an Oxford Instruments MQC+ benchtop NMR analyser with a resonant frequency of 23 MHz operated 25 °C and 37 °C. For the measurement of T_1, the standard inversion-recovery method was employed with a typical 90° pulse calibration of 250 μs with 4 scans per experiment; for T_2, the Carr-Purcell-Meiboom-Gill (CPMG) method was used with 4 scans per experiment. A minimum of 3 different concentrations of stable nanoparticle samples were prepared and relaxation time measured for each sample. r_1 and r_2 relaxivity values were calculated from curves plotted of R_1 ($1/T_1$, s^{-1}) or R_2 ($1/T_2$, s^{-1}) vs. [Fe] concentration (mM, as measured by ICP-OES) and analysis of the slope of the line of best fit for each sample, with error measured from measuring a minimum of 3 separately prepared batches of samples.

An ISA Jobin Yvon Ultima 2C Inductively Coupled Plasma-Optical Emission simultaneous/sequential spectrometer (ICP-OES) running at 1 KW power with a 40.68 MHz radiofrequency Argon plasma. Plasma gas flow was 14 L min^{-1}. Nebuliser pressure was 2.6 bar at 1 mL min^{-1} sample flow rate. The spectral line for iron was measured at 259.940 nm. Samples were digested for ICP-OES using hot nitric acid and diluted in ultrapure water prior to analysis. Concentrations as measured by this technique were used to normalize all relaxation data according to Equation (3).

Preparation of poly(2-acrylamido-2-methylpropane sulfonic acid (P(AMPS)

The preparation of poly(2-acrylamido-2-methylpropane sulfonic acid (P(AMPS)), was carried out as detailed by Bray *et al.*[44] Briefly, the chain transfer agent (CTA) BDMAT, the initiator VA-086 (from stock solution at 20.0 mg mL^{-1}), and the monomer AMPS were combined with phosphate buffer tablet solution (0.5 mL), and sodium hydroxide (2.5 mg, 6.3×10^{-2} mmol) in a flask and sealed with a rubber septum. The relative quantities of CTA, initiator, and monomer were adjusted according to the desired degree of polymerisation (see Table S1). The solution was deoxygenated by bubbling through with nitrogen for 10 minutes, and the flask was then placed in a temperature controlled oil bath at the desired temperature (90 °C), for the duration of time required to reach nearly full conversion (~2 hours). At the end of the reaction, the mixture was allowed to cool down at room temperature and then opened to the atmosphere. The quoted number average molecular weight ($M_{n,SEC}$) and dispersity ($Đ$) values of synthesized polymers were determined by conventional calibration using Agilent GPC/SEC software (see Table S1 for further detail).

Preparation of poly(2-acrylamido-2-methylpropane sulfonic acid (P(AMPS)) Stabilised Maghemite/Magnetite Nanoparticles

Three different synthetic polymers were used, each of a different molecular weight ($M_{n,SEC}$ = 8,100, 17,600, or 41,300 g mol^{-1}), and different molar total [Fe]:[polymer] ratios used, as shown in Table 1. The synthetic P(AMPS) was dissolved in 10 mL ultrapure water, and the solution

was subsequently degassed by bubbling with N_2 for 20 mins. Separately, $FeCl_2 \cdot 4H_2O$ and $FeCl_3 \cdot 6H_2O$ (varied total concentration according to Table 1 but maintained at a 1:2 molar ratio) was dissolved in 50 mL ultrapure water which had already been degassed by bubbling with N_2 for 20 mins (final concentrations provided in Table S2, SI). The P(AMPS) solution was added to the $Fe^{2+/3+}$ solution with the N_2 atmosphere maintained. NH_4OH (1 M) was added in 0.5 mL aliquots until the pH was measured to be in the range 9–10. The reaction was stirred at 40 °C for 2 hours. The resulting black/brown precipitate was washed with ultrapure water using centrifugation until pH neutral. The neutral washings were retained for DLS, TEM and relaxometric analysis.

Characterisation of Haemolytic Behaviour

Defibrinated sheep blood (2 mL) was divided between two 1.5 mL Eppendorf tubes (1 mL each) and centrifuged at 4500 *g*/8200 RPM in a mini spin Eppendorf centrifuge for 1 minute. The supernatant was removed and replaced with 800 µL phosphate buffered saline (PBS), in which the pellet was resuspended using sonication. This was repeated a minimum of 5 times, until the supernatant became colourless. The red blood cell suspension was diluted 1:150 (by volume) in PBS. Samples A–E were diluted in ultrapure water to make concentrations of 0.5 mg mL^{-1}, 0.1 mg mL^{-1}, 0.05 mg mL^{-1}, and 0.01 mg mL^{-1}. 20 µL of each suspension was added to 380 µL of diluted red blood cells making final concentrations of 10, 2, 1, and 0.2 µg mL^{-1}. Negative controls of 20 µL PBS and ultrapure H_2O, and a 100% positive control of 1% Triton-X in PBS was prepared. The diluted red blood cell mixtures were incubated at 37 °C for 1 hour. All samples were prepared in triplicate; values provided as mean of triplicates with error derived from standard deviation. Particle blood mixtures were separated by centrifugation for 5 minutes before 250 µL of the supernatant was removed and transferred to a 96 well plate and the absorbance measured across the range 350–700 nm using a Molecular Devices SpectraMax Plus 384 plate reader. The average peak max value for the PBS negative control value was subtracted from the nanoparticles peak max values and divided by the average Triton-X positive control value to give % haemolysis.

Results and Discussion

Maghemite/magnetite nanoparticles stabilised with P(AMPS) polymer were prepared using an *in-situ* co-precipitation technique, as described in the Experimental section. Briefly, P(AMPS) of three different number average molecular weights ($M_{n,SEC}$ values of 8,100, 17,600, or 41,300 g mol^{-1} with $Đ$ of 1.10, 1.16 and 1.51, respectively) were initially prepared and characterised using size exclusion chromatography (Figure S1 and Table S1, Supporting Information) using a previously published approach.[44] Stabilised maghemite/magnetite nanoparticles were produced by the co-precipitation of Fe^{3+} and Fe^{2+} salts (at a molar ratio of 2:1) in the presence of the P(AMPS) polymers, initiated by the addition of ammonium hydroxide (Figure 1). In order to probe the effect of nanoparticle seeding density

along the polymer chain lengths on MRI contrast enhancement performance, composites were prepared with varied total [Fe]:[P(AMPS)] molar ratios of 100:1, 2,500:1 and 6,250:1, using P(AMPS) with a $M_{n,SEC}$ of 8,100 g mol^{-1} to produce samples A, B, and C respectively (Table 1 and Figure 1). In order to probe the impact of increasing polymer molecular weight, and thus chain length, on particle seeding density, and corresponding MRI behaviour, P(AMPS) stabilised maghemite/magnetite nanoparticles were also prepared using different polymer chain lengths at a constant [Fe]:[P(AMPS)] molar ratio of 6,250:1 (samples D, and E, using polymers with $M_{n,SEC}$ 17,600, and 41,300 g mol^{-1}, respectively, Table 1 and Figure 1).

Table 1. Molar ratios used during preparation of poly(2-acrylamido-2-methylpropane) sulfonate (P(AMPS)) stabilised maghemite/magnetite nanoparticles and resulting characterisation data.

Sample	Total [Fe]:[P(AMPS)] ratio[a]	$M_{n,SEC}$[b] (g mol^{-1})	d_{hyd}[c] (nm) [PDI]	ζ-pot[c] (mV)	d_{core}[d] (nm)	M_s[d] (emu g^{-1} sample)
A	100:1	8,100	255.7±11.0 [0.347]	-25.7±7.5	12.6±3.2	71.8
B	2,500:1	8,100	142.8±33.4 [0.370]	-13.2±2.1	12.9±2.8	70.8
C	6,250:1	8,100	127.3±5.6 [0.319]	-23.5±1.7	11.0±2.4	72.8
D	6,250:1	17,600	167.4±10.4 [0.292]	-20.7±1.7	13.9±5.3	70.9
E	6,250:1	41,300	105.2±15.1 [0.298]	-15.3±1.2	12.8±3.2	71.7

[a] Total initial concentration of reagents (see Table S2 for more information); [b] $M_{n,SEC}$ is number average molecular weight of the P(AMPS) as measured using aqueous size exclusion chromatography (SEC); [c] hydrodynamic diameter (d_{hyd}), zeta potential (ζ-pot) and polydispersity index (PDI) of aqueous colloids measured using dynamic light scattering, with the mean of 4 measurements given (error represents the standard deviation); [d] d_{core} is the average particle size calculated by measuring >100 particles as imaged using transmission electron microscopy with the error representing standard deviation; [e] magnetisation (M_s) at 15 kOe, measured per total mass of solid sample.

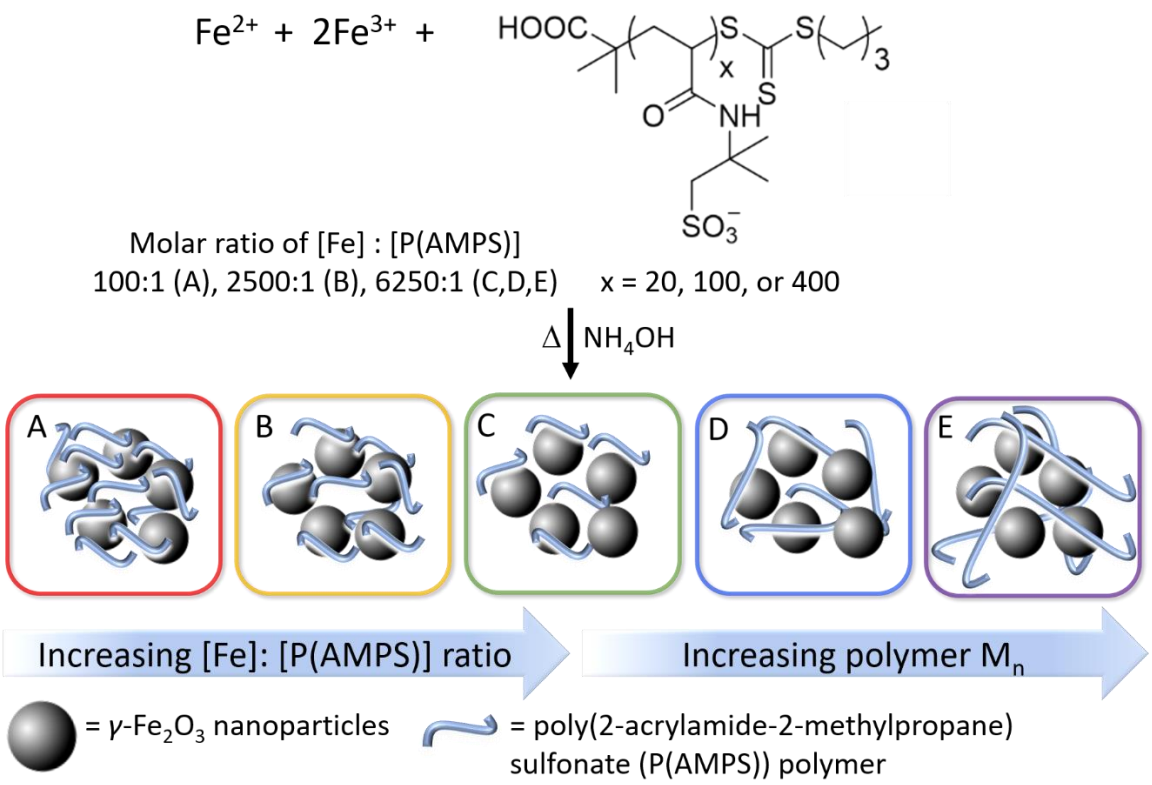

Figure 1. Schematic representation of the preparation of poly(2-acrylamido-2-methylpropane) sulfonate (P(AMPS)) stabilised maghemite/magnetite nanoparticles, with different polymer molecular weights ($M_{n,SEC}$ = 8,100, 17,600, or 41,300 g mol^{-1}) and molar [Fe]:[P(AMPS)] ratios, as shown in Table 1.

Physical and Structural Characterisation

Transmission electron microscopy (TEM) of P(AMPS) stabilised colloids showed aggregates of discrete particles with mean core diameters ranging 11.0–13.5 nm (Figure 2); sizes (Table 1) were within error of one other and not impacted by varying [Fe]:[P(AMPS)] ratio. Nanoparticles demonstrated alignment parallel with an applied magnetic field (2250 Gauss field applied during sample deposition, Figure S2, SI), behaviour attributed to the templating properties of the sulfonate backbone of the polymer chains, which has been previously observed for similarly prepared biopolymer-stabilised magnetic nanoparticles.[30,43,52]

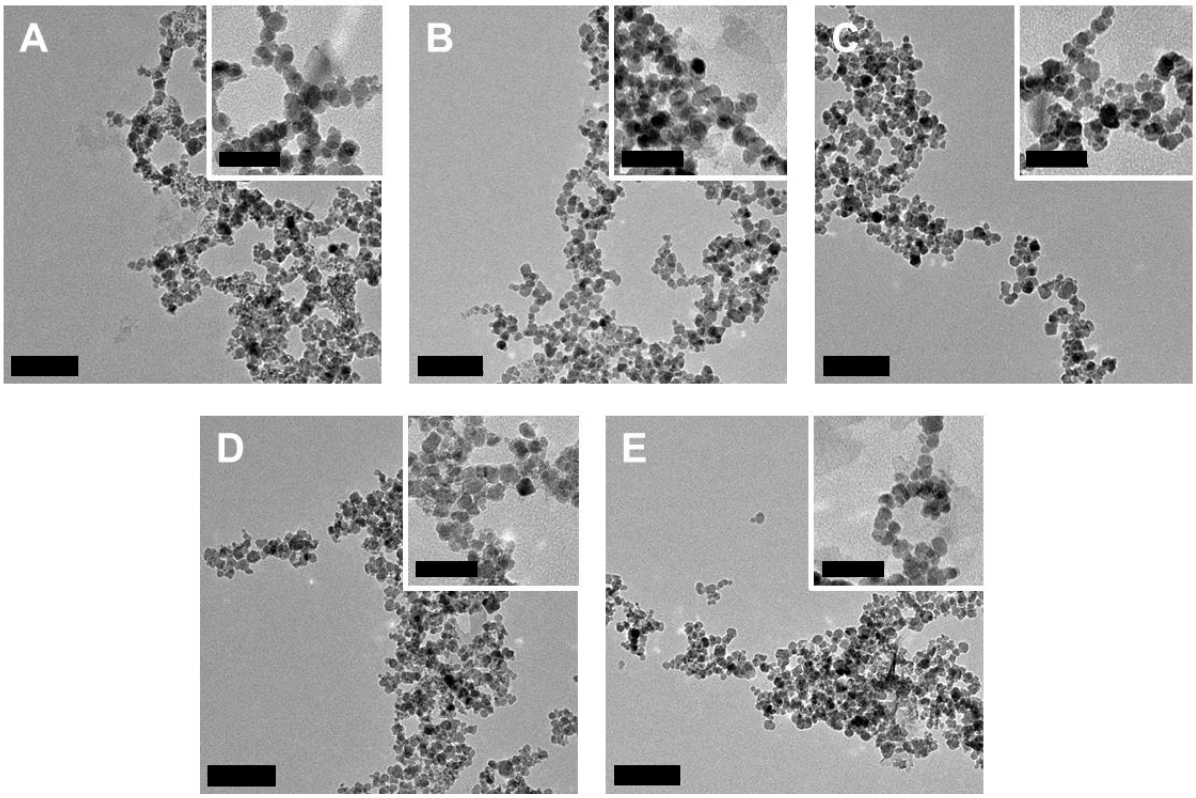

Figure 2. Transmission electron microscopy images of P(AMPS) stabilised maghemite/magnetite nanoparticles, labelled according to Table 1 (d_{core} = 11.0 ± 2.4; 13.9 ± 5.3; 12.8 ± 3.2; 12.9 ± 2.8; 12.6 ± 3.2 nm for samples A–E, respectively). Scale bar 100 nm. Insets show high magnification images of corresponding samples, scale bar 50 nm.

Aqueous hydrodynamic diameters (d_{hyd}) as measured by dynamic light scattering (DLS) (Table 1) were in the range 106–256 nm. These values were significantly larger than core particle sizes as measured by TEM, as expected and previously observed, due to the presence of hydrogen bonding and van der Waals forces associated with the polymer stabilisation of the colloids.[30,42] The d_{hyd} values obtained are larger than similarly prepared iron oxide nanoparticles (for example, heparin-stabilised Fe_3O_4 particles which demonstrated d_{hyd} of ~40 nm for d_{core} 9.0 nm nanoparticles),[30] indicative of larger aqueous clusters of nanocomposites herein. It is notable that the measured d_{hyd} values do not appear to correlate to the size of the P(AMPS) polymer chains, likely due to the low concentrations of the measured samples, and high degree of cross-linking and interactions between neighbouring particles. It is important to note that as the measurements were carried out on stable suspensions following copious washing procedures resulting in different concentrations for each sample, the d_{hyd} values obtained by DLS cannot be directly compared with one another, and thus no trends can be assigned. Differences in hydrodynamic sizes observed are likely due to the large differences in polymer and particle concentrations leading to differences in their cross-linking and Brownian motion behaviour, a well-known phenomenon.[53,54] The impact of the concentration of a suspension of nanoparticles and specifically the observed d_{hyd} is also well documented.[55,56]. The polydispersity index (PDI) quantifies the broadness of distribution of d_{hyd} and is used to estimate the monodispersity and homogeneity of a

colloidal sample. Despite the cross-linking that one would expect from the presence of the polymer species in these nanocomposites, PDI values within the range 0.292–0.370 are indicative of their monodispersity. Zeta potential (ζ-pot) measurements showed all samples to be negatively charged, due to iron oxide particle surface hydroxyl groups (confirmed by IR, *vide infra*), as well as the negatively charged P(AMPS) stabiliser.

Small-angle X-ray scattering (SAXS) was performed on aqueous suspensions of the stabilised particles in order to gain further insight into the colloidal conformation adopted by these nanostructures in suspension. SAXS patterns obtained for all samples show similar trends; the lack of an observable Guinier region within the achievable Q range indicates the formation of relatively large colloidal suspensions in all cases, limiting the capability of SAXS to provide information describing the overall size of the aggregates formed by this system (Figure 3). In order to extract structural information from these SAXS patterns, parameters of a model describing the aggregation of primary spherical particles into a fractal-like cluster were fit to the experimental data, as has been previously been performed with similar systems.[57] A detailed description of this model has been reported previously.[49] Briefly, the fractal dimension represents the self-similarity of the aggregate. Here, we interpret this as a measure of the degree of clustering of individual maghemite/magnetite nanoparticles, where the radius of the clustered aggregate is described by the correlation length.

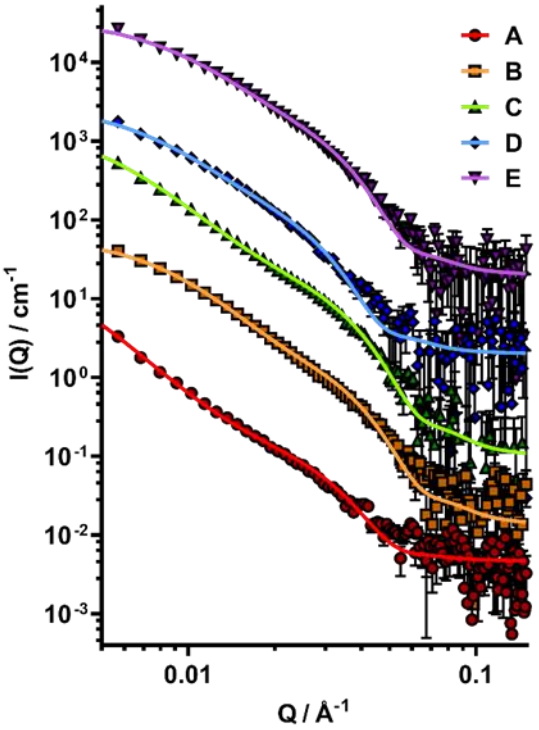

Figure 3. Small-angle X-ray scattering (SAXS) data (points) for aqueous suspensions of P(AMPS) stabilised aggregates of maghemite/magnetite nanoparticles A–E with corresponding fits (lines) to models describing fractal-like clusters of spherical particles.

The parameters obtained from these fitting procedures are displayed in Table 2. In all cases, the maghemite/magnetite nanoparticles radii are similar to those determined by TEM. Comparing samples A and B, as the ratio of [Fe]:[P(AMPS)] increased, an initial increase in fractal dimension can be observed accompanying a decrease in the correlation length. This indicates the particles compact into smaller, more highly clustered aggregates. When the [Fe]:[P(AMPS)] ratio is further increased (sample C), a swelling of the aggregate can be observed with a decreased clustering of maghemite/magnetite nanoparticles. This suggests an optimum ratio of nanoparticles to P(AMPS) is required to produce the most highly clustered aggregates. When considering the polyelectrolyte nature of P(AMPS), we propose that electrostatic repulsion between polymer chains is not countered by the low relative nanoparticle concentration in sample A, leading to swelling described by the larger correlation length and decreased fractal dimension. Similarly, sample C was prepared at the highest [Fe]:[P(AMPS)] ratio in this series. In this case, we propose that the capacity of the polymers to stabilise the maghemite/magnetite nanoparticles has been exceeded, potentially leading to electrostatic repulsion between nanoparticles. As the M_n of P(AMPS) is increased at a constant [Fe]:[P(AMPS)] ratio (samples C, D and E), a decrease in the correlation length can be observed. This suggests that an increase in M_n of P(AMPS) increases the stabilising effect on the nanoparticles leading to the formation of smaller aggregates. Interestingly, the fractal dimension initially increases then appears to stabilise close to the maximum value observed for sample B. This suggests that maghemite/magnetite nanoparticles partition amongst the available P(AMPS) at an apparently optimal compactness.

Table 2. Structural parameters obtained through fitting of SAXS data of aqueous suspensions of P(AMPS) stabilised aggregates of maghemite/magnetite nanoparticles to a model describing fractal-like clusters of spherical particles. Quoted errors represent the standard error associated with the fitted parameter. Values marked with * were held as constant throughout the fitting procedure.

Sample	Volume Fraction ($\times 10^{-6}$)	Iron Oxide NP Radius (Å)	Radial Polydispersity	Fractal Dimension	Correlation Length, (Å)
A	0.8 ± 0.01	70 ± 1	0.2*	2.90 ± 0.01	335 ± 15
B	1.9 ± 0.01	62 ± 1	0.2*	3.47 ± 0.03	85 ± 1
C	1.6 ± 0.01	64 ± 1	0.2*	2.98 ± 0.01	170 ± 3
D	0.7 ± 0.01	83 ± 1	0.2*	3.30 ± 0.09	101 ± 6
E	1.5 ± 0.01	69 ± 1	0.2*	3.32 ± 0.05	80 ± 2

Vibrating sample magnetometry measured between −15 kOe and 15 kOe exhibited typical superparamagnetic behaviour for all samples, with no magnetic hysteresis, and magnetisation values (M_s) in the range 70.9–72.8 emu g^{-1} (see Table 1 and Figure S3, SI). Room temperature (295 ± 5 K) ^{57}Fe Mössbauer spectroscopy (Figure 4a) produced spectra comprising magnetically spilt sextets, characteristic of particles magnetically blocked on the Mössbauer timescale (approx. 1 ns). Best fits to the spectra were obtained using the model independent 'centre of gravity' method to evaluate α, the numerical proportion of Fe atoms in the magnetite environment, with Voigtian line shapes found to obtain the best fit to the spectrum.[51] We see that, within the value of uncertainty for all samples,

calculated according to Fock *et al.* 2016,[58] the value of α is ca. 0.11, (Figure 4b and Table S3), which is indicative of maghemite rich iron oxide cores, with some magnetite character. Significant differences in the shape of the spectra are observed that correlate to both the amount and length of the P(AMPS) polymer used within the synthesis. For samples A, B and C – across which the iron to polymer ratio increases (see Figure 1 and Table 1) – we see significant changes in both the mean static hyperfine field, <*H*>, as well as in the distribution, *P*(H) (Figure 4c). Values obtained for the mean static hyperfine field of A–E are summarized in Table S3, SI. As the ratio of iron increases, <*H*> decreases from 409 kOe to 375 kOe, which we suggest is a result of the increasing frustration of the cores due to structural confinements associated with the increasing amount of iron within the particle, and which is likely to cause clustering of the cores leading to a corresponding alignment along a magnetic easy axis.

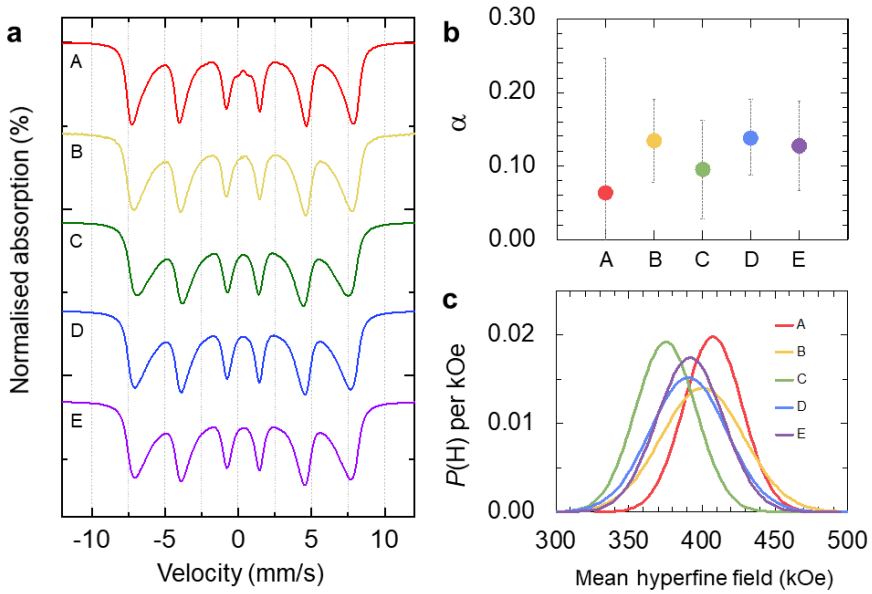

Figure 4. a) Room temperature ^{57}Fe Mössbauer spectra of dried powder samples mixed with sucrose and best fits to the observed spectra (lines) obtained using the 'centre of gravity' method. All best fits were obtained using Voigtian lines (Gaussian distributions of Lorentzian lines); b) Comparison of the best fit values of spectra α, the numerical proportion of Fe atoms in a magnetite environment, for the five samples with corresponding uncertainty values obtained for each spectrum represented by error bars; c) Hyperfine field distribution (*P*(H)) of each of the room temperature spectra shown in (a).

As the length of P(AMPS) increases between samples C to E, we see a slight restructuring of the cores within these clusters, indicated by the slight increase in the mean hyperfine field, and which we suggest gives the iron oxide cores more freedom to re-orientate, which in turn reduces the amount of frustration in the system.

Raman spectroscopy of P(AMPS) stabilised maghemite/magnetite nanoparticles featured a large peak at 670 cm^{-1} and shoulder at 702 cm^{-1} indicating the A_{1g} modes of magnetite and maghemite respectively (Figure S4, SI).[59,60] A broad peak at 368 cm^{-1} represents the T_{2g} mode of maghemite, and another at 494 cm^{-1}, attributed to the E_g mode of maghemite.[59,60] The presence of both the magnetite

and maghemite phase is consistent with room temperature ^{57}Fe Mössbauer spectroscopy analysis. Powder X-ray diffraction (P-XRD) confirmed the characteristic cubic structure of maghemite, with reflections at 13.8°, 16.2°, 19.6°, 25.5°, and 27.8° readily indexed to the (220), (311), (400), (511), and (440) planes of the cubic lattice inverse spinel type iron oxides (Figure S5, SI).[61] Based on the evidence provided by XRD, Raman, and Mössbauer spectroscopy, the particles are clearly present as a mixed phase of material, consisting of the inverse spinel iron oxides maghemite and magnetite, with their relative quantities found to be approximately 89 % maghemite and 11 % magnetite. As a result, the magnetic cores of this nanocomposite are referred to as maghemite/magnetite nanoparticles throughout.

Infrared (IR) spectroscopy confirmed the presence of the stabilising P(AMPS) on the maghemite nanoparticles (Figure S6, SI). The stretches between 3600–3000 cm^{-1} (representing OH stretching vibrations from surface hydroxyl groups and physisorbed water groups), and the stretch at 650–500 cm^{-1} (correlating to the Fe–O stretch) are observed for the P(AMPS) stabilised nanoparticles.[52] The stabilised nanoparticles also exhibited stretches at 1370–1340 cm^{-1} and 1080–1030 cm^{-1}, indicative of the O=S=O and C=S stretching vibrations, respectively, of functional groups on the P(AMPS) chains.[52]

Relaxometry Studies

Nuclear magnetic dispersion (NMRD) analysis is a variable field relaxometry technique which is useful in the analysis of magnetic contrast agents.[6,29,30,36] It measures the longitudinal proton relaxation rate enhancement (r_1) of a colloidal system at multiple frequencies, providing insight into relaxation properties and the dynamic local environment of water nearby a contrast agent species. Such behaviour is influenced by the magnetic properties of a particle and coupled magnetic interactions with one another and their surroundings. The water relaxation rate enhancement per mM concentration of contrast agent, or relaxivity, is defined by Equation (3).

$$r_{1,2} = \frac{R_{1,2,obs} - R_{1,2,sol}}{[CA]} \quad (3)$$

Where $R_{1,2,obs}$ is the observed relaxation rate of the agent in aqueous suspension ($R_{1,2} = 1/T_{1,2}$, where T_1 is the longitudinal relaxation time and T_2 is the transverse relaxation time of water protons), $R_{1,2,sol}$ is the relaxation rate of the unaltered solvent system (*i.e.* in the absence of contrast agent) and [CA] is the mM concentration of the contrast agent in suspension, as measured using inductively coupled plasma optical emission spectroscopy (ICP-OES).

NMRD analysis of aqueous suspensions of the P(AMPS) stabilised maghemite/magnetite nanoparticles is displayed in Figure 5a. At magnetic field strengths of B_0 > 0.2 T (or > 10 MHz), relaxation behaviour is dominated by Curie relaxation, a phenomenon resulting from the induction of a local magnetic field through the application of an external field on the superparamagnetic nanoparticles, and the resultant interactions between water protons and these local magnetic fields.[62] Relaxation at

these field strengths is determined primarily by the strength of the magnetic moments and water diffusional correlation times around magnetic particle cores and therefore tends to correlate to the particle size, d_{core}.[30,62] As d_{core} is similar for samples A–E (Table 1), the NMRD profiles converge at > 10 MHz, as seen in Figure 5a. At lower frequencies (< 10 MHz), the Curie component of relaxation is lost and Néel relaxation (the random fluctuation of magnetic moments) dominates. The seminal model by Roch, Muller, and Gillis first detailed proton relaxation induced by superparamagnetic particles, with profiles that featured a low field plateau (or dispersion), a mid-field peak (ν_{max}), and a decrease in longitudinal relaxivity at higher field strengths.[62] In their model, as the diameter of the magnetic nanoparticles increased, ν_{max} shifted to lower frequencies and low field r_1 relaxivities (at 0.01 MHz) increased, indicative of an increase in the magnetocrystalline anisotropy linked to particle size. For the samples produced herein, ν_{max} is shifted to lower frequencies, and r_1 is greatly increased at low Larmor frequencies. As the core sizes of the 5 samples do not differ significantly (Table 1), this observed behaviour is not attributable to this well-modelled size-related increase in the magnetocrystalline anisotropy. Such behaviour, which diverges from the well-accepted superparamagnetic model, has been previously observed for clustered materials formed from core-shell,[63] and multi-core iron oxide nanoparticles,[64] as well as for iron oxide nanoparticles seeded along biopolymers, such as denatured DNA strands,[43] and fatty acids.[65]

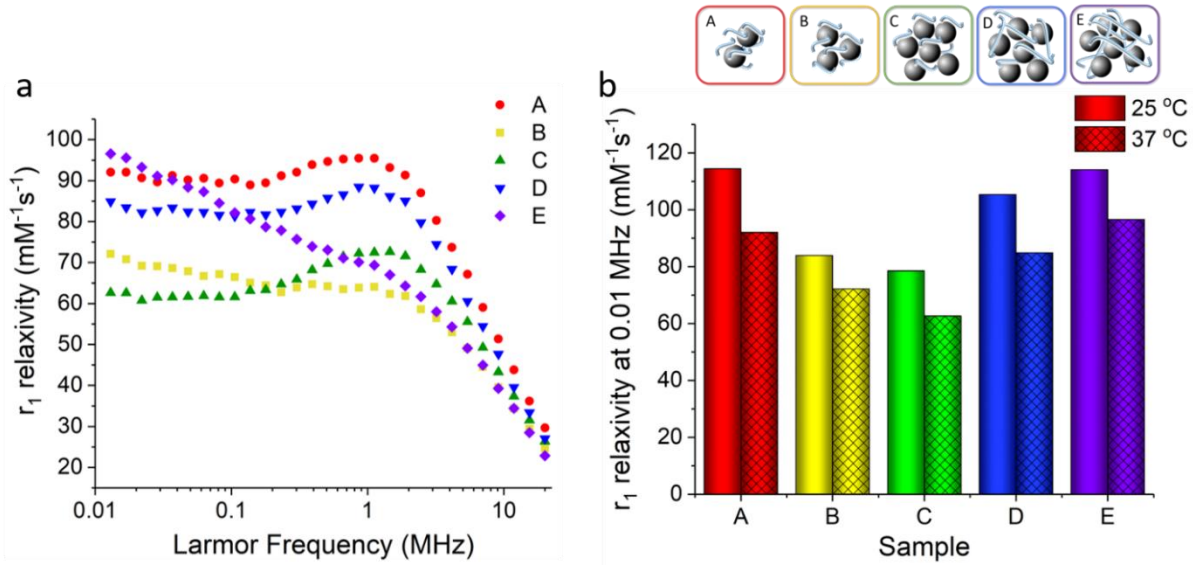

Figure 5. a) ^{1}H NMRD profiles of longitudinal relaxivity (r_1) of P(AMPS) stabilised maghemite/magnetite nanoparticles in 0.1% Xanthan gum, measured at 37 °C; b) Longitudinal relaxivity (r_1) at 0.01 MHz of P(AMPS) stabilised maghemite/magnetite in 0.1 % Xanthan gum, measured at 25 °C and 37 °C. Data points each represent a single measurement.

A model for the effect of agglomeration of superparamagnetic particles on r_1 has been developed by Gillis *et al.*, demonstrating aggregation-induced changes in low frequency dispersion and ν_{max} in NMRD profiles.[66] In that work, it was noted that agglomeration resulted in an overall decrease

in longitudinal relaxivity, due to reduced total surface area of particles available for important, diffusive interactions with surrounding water protons. However, this is clearly not the case herein for samples A–E, where absolute r_1 values at low frequency remain extremely high (Figure 5b). This observed strong relaxation rate enhancement is attributed to the hydrated nature of the polymer-stabilizing species, which facilitates water access to all available particle surface areas, overcoming these previously observed reductions in relaxivity. Bio-heparin stabilized iron oxide particles have similarly exhibited enhanced r_1 relaxivities at low frequencies, behaviour attributed to increased anisotropy arising from interactions between particles clustered along the polymer backbone.[30] Such high low field relaxivities are supported by Lévy *et al.*, who established that the intrinsic magnetic properties of multi-core or clustered nanoparticles results in large relaxivity enhancements at low field strengths due to slowing of the dynamics of the magnetic moments (*i.e.* progressive blocking of Néel fluctuations due to local magneto-anisotropy).[64,67] Clustering-enhanced relaxation effects have also been observed for multi-core iron oxide nanoparticles, including 'nanoflower' structures (composed of an assembly of magnetic cores).[64,68] Herein, cross linking between neighbouring P(AMPS) polymer chains result in the formation of effective "multi-core like" nanostructures in suspension, and supports the observed strong low field relaxivities, which closely resemble the multi-core model proposed by Lévy *et al*.

In our samples, this phenomenon is likely due to the propensity for colloidal polymers to adopt different energetically-favourable conformations (brush, mushroom, coil, *etc.*) when in aqueous suspension.[69,70] This dynamic behaviour may bring the iron oxide cores (associated with negative polyelectrolyte backbones) close together, resulting in this "multi-core like" behaviour, whilst the hydrophilic nature of the polymers ensures excellent water diffusivity, avoiding reduced relaxivities as a result of agglomeration and hence restricted water access, as had been observed by Gillis *et al*.[66] Indeed, the templating nature of the polyelectrolyte species and nanoparticle seeding behaviour it encourages may serve to impact the adopted conformation of the polymer chains, with nanoparticles shown to have profound effects on the motion and molecular conformation of polymers in polymer-nanoparticle composites.[71,72]

This dynamic behaviour appears to impact the low frequency r_1 of the samples prepared herein (Figure 5b). More dynamic and flexible samples, possessing higher amounts and longer chain lengths of polymers possess the highest low field relaxivities (*e.g.* samples A and E), whereas samples with high densities of iron oxide particles and smaller polymer chain lengths (*e.g.* sample C) have lower low frequency r_1 values, due to their inherently lower dynamic flexibility, a well-accepted phenomenon in aqueous systems. Herein, increased flexibility enhances hydration and clustering of the iron oxide particles, making it more effective and hence resulting in the high r_1 relaxation enhancement. This behaviour is supported by the SAXS data discussed previously, in which the fractal-like aggregation of iron particles are concurrent with the idea that there are varying degrees of 'clustering' with these multi-core like structures leading to differences in the distance between magnetic cores, and interparticle

interactions which are known to boost relaxation properties. Similar trends in NMRD relaxation were observed at 25 °C (Figure S7, SI).

Table 3. Summary of r_1 and r_2 relaxometric properties of P(AMPS) stabilised maghemite/magnetite nanoparticle samples (A–E) measured at a single field strength (23 MHz) and at temperatures of 25 °C and 37 °C.

Sample	r_2 ($mM^{-1}s^{-1}$)		r_1 ($mM^{-1}s^{-1}$)		r_2/r_1	
	25 °C	37 °C	25 °C	37 °C	25 °C	37 °C
A	331.5 ± 13.3	312.4 ± 31.4	40.1 ± 1.6	41.0 ± 1.5	8.3	7.6
B	363.4 ± 30.8	318.5 ± 21.9	34.6 ± 1.4	33.1 ± 2.9	10.5	9.6
C	434.2 ± 59.4	386.2 ± 32.2	42.7 ± 1.9	41.2 ± 0.2	10.2	9.4
D	431.0 ± 25.4	386.4 ± 17.4	39.9 ± 1.7	39.3 ± 1.5	10.8	9.8
E	367.1 ± 18.7	318.5 ± 19.4	40.3 ± 3.3	39.9 ± 3.3	9.2	8.0

Values presented are the mean and standard deviation of the measured relaxivities of a minimum of 3 replicates for each sample (A–E).

The transverse relaxivities (r_2) of aqueous colloids of the P(AMPS) stabilised maghemite/magnetite nanoparticles were additionally measured at a single field strength of 23 MHz to assess their efficacy as negative contrast agents (Table 3). Unlike longitudinal relaxation (measured in NMRD analysis), transverse relaxation is not proportional to Larmor frequency, as the mechanism for relaxation is reliant on the dephasing of the proton spins and is dominated by outer sphere interactions. r_2 relaxivities showed general correlation with the cluster size, with smaller aggregates (following fractal dimension according to SAXS, as previously discussed) demonstrating lower r_2 relaxivities due to their overall lower magnetic moment. All samples demonstrated extremely high r_2 values, ranging 331–435 $mM^{-1}s^{-1}$ at 25°C, far exceeding that of clinical analogues such as Feridex® (r_2 = 120 $mM^{-1}s^{-1}$ at 25 °C and 20 MHz).[15] At 37 °C, r_2 values for all samples are slightly reduced, due to the thermal activation of water molecules and its subsequent impact on the diffusional correlation time around the particle cores, a well-documented phenomenon.[73] High r_2/r_1 ratios, ranging 8.3–10.8 at 25 °C, indicated their strong potential as negative CAs.

Haemolytic Activity

Haemocompatibility is crucial for *in vivo* bio-applications of nanomaterials, particularly if the nanocomposite is to come into contact with blood through intravenous clinical administration.[74,75] Due to their poor colloidal stability, uncoated iron oxide nanoparticles have a high tendency for agglomeration under physiological conditions, and have shown considerable damage to red blood cells and their membranes, resulting in haemolysis.[76,77,78] To quantitatively determine the blood compatibility of the nanocomposites described herein, a widely used haemolysis assay was carried out, adapted from methods detailed in the literature.[45] Briefly, the release of haemoglobin from ovine red blood cells was measured using UV-vis spectroscopy after incubation with the P(AMPS) stabilised maghemite/magnetite nanoparticles (Figure 6, details in Experimental section). The percentage haemolysis was calculated for different concentrations for each of the 5 samples, with the % haemolysis found to be in the range of 8.1–24.6 %. These results were found to be statistically insignificant with

respect to the negative control of water (P>0.05), therefore demonstrating the good haemocompatibility of the P(AMPS) stabilised nanoparticles. The ability of a coating or stabiliser to improve the haemocompatibility of iron oxide nanoparticles has been well documented in the literature. For example, a study of polyethylenimine (PEI) and polyethylene glycol (PEG) coated SPIONs showed that PEI-coated nanoparticles exhibited severe dose-dependent haemolysis due to formation of large aggregates in the presence of plasma, whilst a PEG coating on SPIONS prevented the formation of such aggregates, resulting in no haemolytic activity.[79] Likewise, a comparison between polyacrylic acid-, hyaluronic acid-, and chitosan-modified iron oxide nanoparticles found the chitosan- and hyaluronic acid-functionalised nanoparticles had superior blood compatibility, behaviour linked to their improved colloidal stability.[76] P(AMPS) has already been demonstrated to have excellent blood compatibility (at concentration ranges of 1–100 μg mL^{-1}, showing % haemolysis 18.2–22.2 %), behaviour linked to its heparin-mimicking properties.[45] As such, it is reasonable to link the excellent blood compatibility observed in the samples herein to the use of the P(AMPS) stabilising agent. However, it is important to note that the concentrations of P(AMPS) present within the nanocomposites prepared in this work are much lower than those used to determine blood compatibility of polymers alone (concentrations presented herein represent complete polymer-nanoparticle composite species). Despite this, it is clear that there is sufficient polymer present to provide excellent blood compatibility. Further, it is interesting to note that the measured haemolysis of the clinically approved anti-coagulant heparin falls within the range observed for the P(AMPS) coated maghemite/magnetite nanoparticles (8.1–24.6 %),[45] emphasising their potential for future safe biomedical application.

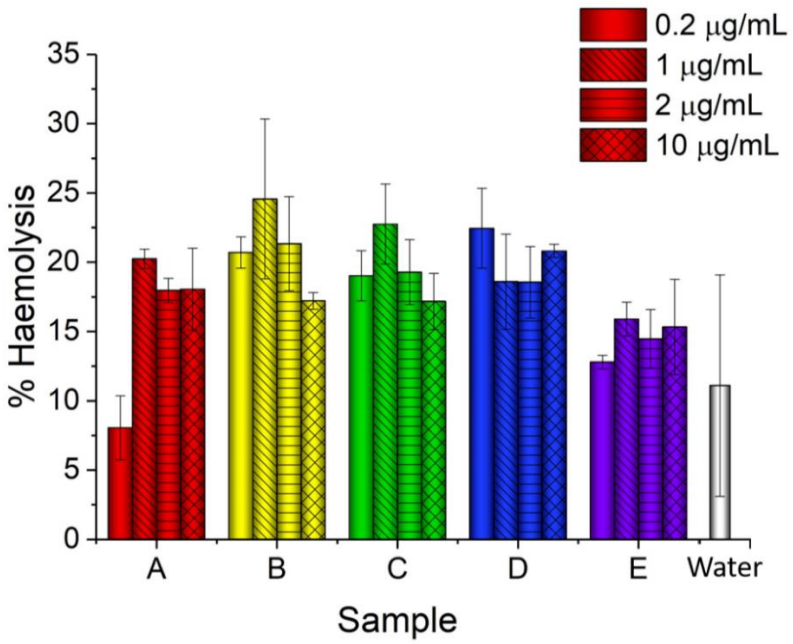

Figure 6. Haemocompatibility of P(AMPS) stabilised maghemite/magnetite nanoparticles (A–E) measured as a percentage with 100 % positive control using 1 % Triton-X in PBS, with water and PBS as negative controls. Figure shows the mean ± standard error of the mean where n = 3.

Conclusion

The ability of polymers to act as stabilisers as well as templating agents in the preparation of colloidal magnetic nanoparticles has been established in the literature in recent years. A number of works have produced nanocomposites with enhanced magnetic relaxation properties due, in part, to template-mediated interparticle interactions, which have been controlled through tuning the seeding density of nanoparticles along polyelectrolyte backbones.[29,30,43] However, despite efforts to tune relaxation behaviour of the nanocomposites, poor polydispersity of commercial polymers hamper the true reproducibility and tunability of these interesting systems, and lack insight into the colloidal behaviour of these interesting systems. Herein, we have utilised a precision-designed poly(2-acrylamido-2-methylpropane sodium sulfonate) (P(AMPS)) polymer with well-defined molecular weights, to produce colloidal magnetic nanocomposites which form clusters of particles in aqueous suspension, thanks to the polymer's controlled number of sulfonate sites guiding seeded nanoparticle growth. This means of control has resulted not only in magnetic nanocomposites with improved relaxometric properties, but has also provided insight into the unique and dynamic colloidal behaviour of this important class of polymer-stabilised MRI contrast agents. Through exploitation of the polymer chains' dynamic flexibility in solution, as well as the density of particles associated with the polymer chains, nanocomposites with different degrees of colloidal clustering behaviour can be produced, which facilitate interparticle interactions vital for boosted proton relaxation. Variable field relaxometry (nuclear magnetic resonance dispersion, NMRD) allowed interpretation of these important interactions, revealing unexpected behaviour, in particular at low field strengths. The loss of a defined ν_{max} and low field dispersion (through increased r_1 in the 0.01–0.1 MHz range), correlates with relaxometric behaviour observed for multi-core magnetic nanoparticles previously modelled in the literature.[64,67,68] Small-angle X-ray scattering confirmed the colloidal properties of these composites in suspension – demonstrating the formation of multi-core clusters of nanoparticles in the samples prepared herein, with the degree of clustering influenced by the [Fe]:[P(AMPS)] ratio, as well as the P(AMPS) M_n, where an increase in chain length resulted in the formation of smaller clusters, which present high low field r_1 relaxivities. Together, this data clearly illustrates the ability to tune the degree of clustering and hence control the MRI behaviour of this family of contrast agents, through modulation of the important interparticle interactions. This work emphasises, for the first time, the necessity to carefully tune all aspects of reagent properties when selecting materials for the production of colloidal nanoparticles for medical applications. High single field r_2 relaxivities (of up to $r_2 = 434.2 \pm 59.4$ $mM^{-1}s^{-1}$ at 23 MHz and 25 °C) far exceed that of clinical analogues such as Feridex ($r_2 = 120$ $mM^{-1}s^{-1}$ at 25 °C and 20 MHz).[15] Alongside excellent MRI contrast potential, low haemolytic activity was measured for all nanocomposites produced, demonstrating the good biocompatibility of the samples.

Collectively, the results demonstrate that judicious choice of polymer, in particular considering polydispersity and polymer chain length, as well as carefully designed composite ratios, are of vital

importance in tailoring the resulting properties of produced colloidal nanocomposites, in particular for biomedical applications such as MRI. Precision designed polymers are ideal for such applications, allowing careful control not only over the well-established importance of interparticle interactions, but also composite flexibility and nanoparticle clustering, which we have demonstrated to play a key role in the resulting MRI contrast behaviour. Future work with this new family of negative MRI contrast agents will focus on further detailing their biological behaviour both *in vitro* and *in vivo*.

Conflicts of Interest

There are no conflicts to declare.

Acknowledgements

The authors acknowledge financial support from the EPSRC (EP/N509577/1, supporting AMK). Thanks to Stelar Srl for NMRD measurements, Steven Huband and the University of Warwick X-ray diffraction Research Technology Platform for SAXS measurements and Professor Quentin Pankhurst for access to TEM at the Royal Institution. This work benefited from the use of the SasView application, originally developed under NSF award DMR-0520547. SasView contains code developed with funding from the European Union's Horizon 2020 research and innovation programme under the SINE2020 project, grant agreement No 654000.

CRediT Statement

Aaron M. King – *Methodology, Formal analysis, Investigation, Writing – original draft, Visualization.*
Caroline Bray – *Investigation, Formal analysis, Resources, Writing – review and editing.*
Stephen C. L. Hall – *Formal analysis, Investigation, Writing – original draft, Visualization.*
Joseph. C. Bear – *Investigation, Formal analysis.*
Lara K. Bogart – *Formal analysis, Investigation, Writing – original draft, Visualization.*
Sebastien Perrier – *Resources, Writing – review and editing, Supervision.*
Gemma-Louise Davies – *Conceptualization, Resources, Writing – review and editing, Supervision, Project administration, Funding acquisition.*

References

1 O. Gleeson, G. L. Davies, A. Peschiulli, R. Tekoriute, Y. K. Gun'Ko and S. J. Connon, *Org. Biomol. Chem.*, 2011, **9**, 7929–7940.

2 J. Wang, S. Zheng, Y. Shao, J. Liu, Z. Xu and D. Zhu, *J. Colloid Interface Sci.*, 2010, **349**, 293–299.

3 G.-L. Davies, J. Govan, R. Tekoriute, R. Serrano-García, H. Nolan, D. Farrell, O. Hajatpour and

Y. K. Gun'ko, *Chem. Sci.*, 2017, **8**, 7758–7764.

4 F. Bertoli, G.-L. Davies, M. P. Monopoli, M. Moloney, Y. K. Gun'ko, A. Salvati and K. A. Dawson, *Small*, 2014, **10**, 3307–3315.

5 H. Lee, E. Sun, D. Ham and R. Weissleder, *Nat. Med.*, 2008, **14**, 869–874.

6 A. Boni, A. M. Basini, L. Capolupo, C. Innocenti, M. Corti, M. Cobianchi, F. Orsini, A. Guerrini, C. Sangregorio and A. Lascialfari, *RSC Adv.*, 2017, **7**, 44104–44111.

7 T. Yin, P. Huang, G. Gao, J. G. Shapter, Y. Shen, R. Sun, C. Yue, C. Zhang, Y. Liu, S. Zhou and D. Cui, *Sci. Rep.*, 2016, **6**, 36187.

8 S. A. McCarthy, G.-L. Davies and Y. K. Gun'ko, *Nat. Protoc.*, 2012, **7**, 1677–1693.

9 G.-L. Davies, I. Kramberger and J. J. Davis, *Chem. Commun.*, 2013, **49**, 9704.

10 H. Bin Na, I. C. Song and T. Hyeon, *Adv. Mater.*, 2009, **21**, 2133–2148.

11 E. J. Werner, A. Datta, C. J. Jocher and K. N. Raymond, *Angew. Chemie Int. Ed.*, 2008, **47**, 8568–8580.

12 P. Caravan, J. J. Ellison, T. J. McMurry and R. B. Lauffer, *Chem. Rev.*, 1999, **99**, 2293–2352.

13 R. Jin, B. Lin, D. Li and H. Ai, *Curr. Opin. Pharmacol.*, 2014, **18**, 18–27.

14 Q. A. Pankhurst, N. T. K. Thanh, S. K. Jones and J. Dobson, *J. Phys. D. Appl. Phys.*, 2009, **42**, 224001.

15 N. Lee, D. Yoo, D. Ling, M. H. Cho, T. Hyeon and J. Cheon, *Chem. Rev.*, 2015, **115**, 10637–10689.

16 J. Ramalho, R. C. Semelka, M. Ramalho, R. H. Nunes, M. AlObaidy and M. Castillo, *Am. J. Neuroradiol.*, 2016, **37**, 1192–1198.

17 E. A. Sadowski, L. K. Bennett, M. R. Chan, A. L. Wentland, A. L. Garrett, R. W. Garrett and A. Djamali, *Radiology*, 2007, **243**, 148–157.

18 K. Müller, J. N. Skepper, M. Posfai, R. Trivedi, S. Howarth, C. Corot, E. Lancelot, P. W. Thompson, A. P. Brown and J. H. Gillard, *Biomaterials*, 2007, **28**, 1629–1642.

19 S. Tong, S. Hou, Z. Zheng, J. Zhou and G. Bao, *Nano Lett.*, 2010, **10**, 4607–4613.

20 J. Huang, L. Wang, R. Lin, A. Y. Wang, L. Yang, M. Kuang, W. Qian and H. Mao, *ACS Appl. Mater. Interfaces*, 2013, **5**, 4632–4639.

21 N. Lewinski, V. Colvin and R. Drezek, *Small*, 2008, **4**, 26–49.

22 A. M. G. C. Dias, A. Hussain, A. S. Marcos and A. C. A. Roque, *Biotechnol. Adv.*, 2011, **29**, 142–155.

23 H. Wang, A. Mararenko, G. Cao, Z. Gai, K. Hong, P. Banerjee and S. Zhou, *ACS Appl. Mater. Interfaces*, 2014, **6**, 15309–15317.

24 A. Hervault, A. E. Dunn, M. Lim, C. Boyer, D. Mott, S. Maenosono and N. T. K. Thanh, *Nanoscale*, 2016, **8**, 12152–12161.

25 C. Blanco-Andujar, D. Ortega, P. Southern, Q. A. Pankhurst and N. T. K. Thanh, *Nanoscale*, 2015, **7**, 1768–1775.

26 R. Hachani, M. Lowdell, M. Birchall and N. T. K. Thanh, *Nanoscale*, 2013, **5**, 11362–11373.

27 F. Sousa, B. Sanavio, A. Saccani, Y. Tang, I. Zucca, T. M. Carney, A. Mastropietro, P. H. Jacob Silva, R. P. Carney, K. Schenk, A. O. Omrani, P. Huang, L. Yang, H. M. Rønnow, F. Stellacci and S. Krol, *Bioconjug. Chem.*, 2017, **28**, 161–170.

28 L. Yang, C. Sun, H. Lin, X. Gong, T. Zhou, W.-T. Deng, Z. Chen and J. Gao, *Chem. Mater.*, 2019, **31**, 1381–1390.

29 G.-L. Davies, S. A. Corr, C. J. Meledandri, L. Briode, D. F. Brougham and Y. K. Gun'ko, *ChemPhysChem*, 2011, **12**, 772–776.

30 L. Ternent, D. A. Mayoh, M. R. Lees and G.-L. Davies, *J. Mater. Chem. B*, 2016, **4**, 3065–3074.

31 J. Reguera, D. Jiménez de Aberasturi, M. Henriksen-Lacey, J. Langer, A. Espinosa, B. Szczupak, C. Wilhelm and L. M. Liz-Marzán, *Nanoscale*, 2017, **9**, 9467–9480.

32 C. E. Smith, J. Lee, Y. Seo, N. Clay, J. Park, A. Shkumatov, D. Ernenwein, M.-H. Lai, S. Misra, C. E. Sing, B. Andrade, S. C. Zimmerman and H. Kong, *ACS Appl. Mater. Interfaces*, 2017, **9**, 1219–1225.

33 J.-H. Lee, Y.-M. Huh, Y. Jun, J. Seo, J. Jang, H.-T. Song, S. Kim, E.-J. Cho, H.-G. Yoon, J.-S. Suh and J. Cheon, *Nat. Med.*, 2007, **13**, 95–99.

34 N. Lee, Y. Choi, Y. Lee, M. Park, W. K. Moon, S. H. Choi and T. Hyeon, *Nano Lett.*, 2012, **12**, 3127–3131.

35 T. D. T. Nguyen, A. Pitchaimani, C. Ferrel, R. Thakkar and S. Aryal, *Nanoscale*, 2018, **10**, 284–294.

36 Y. Sun, C. Yan, J. Xie, D. Yan, K. Hu, S. Huang, J. Liu, Y. Zhang, N. Gu and F. Xiong, *ACS Appl. Mater. Interfaces*, 2019, **11**, 29536–29548.

37 L. Yang, Z. Wang, L. Ma, A. Li, J. Xin, R. Wei, H. Lin, R. Wang, Z. Chen and J. Gao, *ACS Nano*, 2018, **12**, 4605–4614.

38 F. Hu, Q. Jia, Y. Li and M. Gao, *Nanotechnology*, 2011, **22**, 245604.

39 C. Sun, K. Du, C. Fang, N. Bhattarai, O. Veiseh, F. Kievit, Z. Stephen, D. Lee, R. G. Ellenbogen, B. Ratner and M. Zhang, *ACS Nano*, 2010, **4**, 2402–2410.

40 C. C. Berry, S. Wells, S. Charles and A. S. G. Curtis, *Biomaterials*, 2003, **24**, 4551–4557.

41 A. Villanueva, M. Cañete, A. G. Roca, M. Calero, S. Veintemillas-Verdaguer, C. J. Serna, M. del Puerto Morales and R. Miranda, *Nanotechnology*, 2009, **20**, 115103.

42 S. A. Corr, Y. K. Gun'ko, R. Tekoriute, C. J. Meledandri and D. F. Brougham, *J. Phys. Chem. C*, 2008, **112**, 13324–13327.

43 S. J. Byrne, S. A. Corr, Y. K. Gun'ko, J. M. Kelly, D. F. Brougham and S. Ghosh, *Chem. Commun.*, 2004, **10**, 2560–2561.

44 C. Bray, R. Peltier, H. Kim, A. Mastrangelo and S. Perrier, *Polym. Chem.*, 2017, **8**, 5513–5524.

45 P. Gurnani, C. P. Bray, R. A. E. Richardson, R. Peltier and S. Perrier, *Macromol. Rapid Commun.*, 2019, **40**, 1800314.

46 G. David and J. Pérez, *J. Appl. Crystallogr.*, 2009, **42**, 892–900.

47 F. Zhang, J. Ilavsky, G. G. Long, J. P. G. Quintana, A. J. Allen and P. R. Jemian, in *Metallurgical and Materials Transactions A: Physical Metallurgy and Materials Science*, Springer US, 2010, vol. 41, pp. 1151–1158.

48 M. Doucet, J. H. Cho, A. Gervaise, J. Bakker, W. Bouwman, P. Butler and A. Washington, *SasView Small Angle Scatt. Anal. (version 4.1.2)*, 2017.

49 J. Teixeira, *J. Appl. Crystallogr.*, 1988, **21**, 781–785.

50 K. Lagarec and D. G. Rancourt, *Recoil-Mössbauer Spectr. Anal. Softw. Wind. (version 1.0)*, 1998.

51 J. Fock, L. K. Bogart, D. González-Alonso, J. I. Espeso, M. F. Hansen, M. Varón, C. Frandsen and Q. A. Pankhurst, *J. Phys. D. Appl. Phys.*, 2017, **50**, 265005.

52 S. A. Corr, S. J. Byrne, R. Tekoriute, C. J. Meledandri, D. F. Brougham, M. Lynch, C. Kerskens, L. O'Dwyer and Y. K. Gun'ko, *J. Am. Chem. Soc.*, 2008, **130**, 4214–4215.

53 M. Doi and S. F. Edwards, *J. Chem. Soc. Faraday Trans. 2 Mol. Chem. Phys.*, 1978, **74**, 1789–1801.

54 A. Van Veluwen, H. N. W. Lekkerkerker, C. G. De Kruif and A. Vrij, *Faraday Discuss. Chem. Soc.*, 1987, **83**, 59–67.

55 M. Baalousha, *Sci. Total Environ.*, 2009, **407**, 2093–2101.

56 N. Maximova and O. Dahl, *Curr. Opin. Colloid Interface Sci.*, 2006, 11, 246–266.

57 W. Szczerba, R. Costo, S. Veintemillas-Verdaguer, M. del P. Morales and A. F. Thünemann, *J. Appl. Crystallogr.*, 2017, **50**, 481–488.

58 J. Fock, L. K. Bogart, O. Posth, M. F. Hansen, Q. A. Pankhurst and C. Frandsen, *Hyperfine Interact.*, 2016, **237**, 1–11.

59 M. I. Dar and S. A. Shivashankar, *RSC Adv.*, 2014, **4**, 4105–4113.

60 A. M. Jubb and H. C. Allen, *ACS Appl. Mater. Interfaces*, 2010, **2**, 2804–2812.

61 T. Hyeon, S. S. Lee, J. Park, Y. Chung and H. Bin Na, *J. Am. Chem. Soc.*, 2001, **123**, 12798–12801.

62 A. Roch, R. N. Muller and P. Gillis, *J. Chem. Phys.*, 1999, **110**, 5403–5411.

63 O. B. Miguel, Y. Gossuin, M. P. Morales, P. Gillis, R. N. Muller and S. Veintemillas-Verdaguer, *Magn. Reson. Imaging*, 2007, **25**, 1437–1441.

64 L. Lartigue, P. Hugounenq, D. Alloyeau, S. P. Clarke, M. Lévy, J.-C. Bacri, R. Bazzi, D. F. Brougham, C. Wilhelm and F. Gazeau, *ACS Nano*, 2012, **6**, 10935–10949.

65 S. Ghosh, D. Carty, S. P. Clarke, S. A. Corr, R. Tekoriute, Y. K. Gun'Ko and D. F. Brougham, *Phys. Chem. Chem. Phys.*, 2010, **12**, 14009–14016.

66 A. Roch, Y. Gossuin, R. N. Muller and P. Gillis, *J. Magn. Magn. Mater.*, 2005, **293**, 532–539.

67 M. Lévy, F. Gazeau, C. Wilhelm, S. Neveu, M. Devaud and P. Levitz, *J. Phys. Chem. C*, 2013, **117**, 15369–15374.

68 Y. Javed, L. Lartigue, P. Hugounenq, Q. L. Vuong, Y. Gossuin, R. Bazzi, C. Wilhelm, C. Ricolleau, F. Gazeau and D. Alloyeau, *Small*, 2014, **10**, 3325–3337.

69 D. Sarkar and P. Somasundaran, *Langmuir*, 2004, **20**, 4657–4664.

70 E. P. K. Currie, W. Norde and M. A. C. Cohen Stuart, *Adv. Colloid Interface Sci.*, 2003, **100**–**102**, 205–265.

71 R. Mangal, S. Srivastava and L. A. Archer, *Nat. Commun.*, 2015, **6**, 7198.

72 A. Tuteja, P. M. Duxbury and M. E. Mackay, *Macromolecules*, 2007, **40**, 9427–9434.

73 T. Kawaguchi, A. Yoshino, M. Hasegawa, T. Hanaichi, S. Maruno and N. Adachi, *J. Mater. Sci. Mater. Med.*, 2002, **13**, 113–117.

74 L. E. Wilkins, D. J. Phillips, R. C. Deller, G.-L. Davies and M. I. Gibson, *Carbohydr. Res.*, 2015, **405**, 47–54.

75 J. Li, L. Zheng, H. Cai, W. Sun, M. Shen, G. Zhang and X. Shi, *Biomaterials*, 2013, **34**, 8382–8392.

76 T. Liu, R. Bai, H. Zhou, R. Wang, J. Liu, Y. Zhao and C. Chen, *RSC Adv.*, 2020, **10**, 7559–7569.

77 L. Q. Chen, L. Fang, J. Ling, C. Z. Ding, B. Kang and C. Z. Huang, *Chem. Res. Toxicol.*, 2015, **28**, 501–509.

78 Q. Ran, Y. Xiang, Y. Liu, L. Xiang, F. Li, X. Deng, Y. Xiao, L. Chen, L. Chen and Z. Li, *Sci. Rep.*, 2015, **5**, 1–15.

79 Q. Feng, Y. Liu, J. Huang, K. Chen, J. Huang and K. Xiao, *Sci. Rep.*, 2018, **8**, 1–13.